Coupling to zone-center optical phonons in VSe_2 enhanced by charge density waves

Y. Falke,[1,*] N. Ehlen,[1] G. Marini,[2] A. V. Fedorov,[1,3,4] V. Y. Voroshnin,[3,4] B. V. Senkovskiy,[1] K. Nikonov,[1,5]
M. Hoesch,[6,7] T. K. Kim,[6] L. Petaccia,[8] G. Di Santo,[8] T. Szkopek,[9] G. Profeta,[2,†] and A. Grüneis[1,‡]
[1]*II. Physikalisches Institut, Universität zu Köln, Zülpicher Strasse 77, 50937 Köln, Germany*
[2]*Department of Physical and Chemical Sciences, University of L'Aquila, Via Vetoio 10, I-67100 Coppito, Italy*
[3]*Institute for Solid State Research, Leibniz IFW-Dresden, 01069 Dresden, Germany*
[4]*Helmholtz-Zentrum Berlin für Materialien und Energie, 12489 Berlin, Germany*
[5]*Kurnakov Institute of General and Inorganic Chemistry, Russian Academy of Sciences, 119991 Moscow, Russia*
[6]*Diamond Light Source, Harwell Campus, Didcot, OX11 0DE, United Kingdom*
[7]*DESY Photon Science, Deutsches Elektronen-Synchrotron, Notkestrasse 85, 22607 Hamburg, Germany*
[8]*Elettra Sincrotrone Trieste, Strada Statale 14 km 163.5, 34149 Trieste, Italy*
[9]*McGill University, Department of Electrical and Computer Engineering, H3A 2A7 Montreal, Canada*

(Received 23 May 2021; revised 21 November 2021; accepted 9 December 2021; published 20 December 2021)

We investigate electron-phonon coupling (EPC) in the charge density wave (CDW) phase of VSe_2 by Raman spectroscopy, angle-resolved photoemission spectroscopy (ARPES), and *ab initio* calculations. Zone folding induced by the 4 × 4 in-plane CDW phase promotes the appearance of a Raman peak at $\sim$170 cm^{-1}. The suppression of ARPES intensity in parts of the Fermi surface is also a result of CDW-induced zone folding and anticrossing of the electron energy bands. The appearance of the new Raman peak is in line with the ARPES observation of a kink feature in the spectral function at the same energy. A self-energy analysis yields an EPC constant of $\lambda = 0.3$. Our calculations of the EPC are in excellent agreement and reveal that the kink is caused by several optical phonon branches close in energy. Our paper highlights the CDW phase as a means of inducing EPC pathways to optical phonons that directly affect its Raman spectrum.

DOI: 10.1103/PhysRevB.104.235137

I. INTRODUCTION

Charge density waves (CDWs) in metallic layered transition metal dichalcogenides (TMDCs) are a result of nesting portions of the Fermi surface, strong momentum-dependent electron phonon coupling (EPC), or a combination of both [1,2]. In several TMDCs, the CDW electronic ground state can be easily recognized by spectroscopy. For example, angle-resolved photoemission spectroscopy (ARPES) has been used to observe zone-folded electron energy bands [3] and a CDW gap [4] in 2H-$TiSe_2$ and 2H-$NbSe_2$, respectively. The strong EPC in 2H-$NbSe_2$ has been observed as a kink feature by ARPES [5]. The vibrational properties of TMDCs are also affected by the CDW phase, e.g., 2H-$NbSe_2$ has a new Raman peak appearing in the CDW phase [6].

The spectroscopic properties of the CDW phase of VSe_2 which crystallizes in the 1T polytype are less clear. VSe_2 has CDW transitions at 80 K and 110 K driven by coupling to acoustic phonons [7]. Under pressure, VSe_2 undergoes a structural change and becomes superconducting [8]. The CDW phase below 80 K has a commensurate 4 × 4 × 3 ordering and in the CDW phase between 80 K and 110 K there is a 4 × 4 in-plane and incommensurate out-of-plane ordering [9–11]. The in-plane ordering is consistent with calculations of the susceptibility that peaks at a quarter of the reciprocal in-plane lattice vector [12]. EPC has not been observed in all previous ARPES experiments [13–15] and the estimation of the partial CDW gap of $\Delta = 80 - 100$ meV [13] from ARPES is not in agreement with scanning tunneling spectroscopy measurements yielding $2\Delta = 24 \pm 6$ meV [16]. Moreover, the in-plane location of the CDW gap is known to be at the Brillouin zone (BZ) edge but the precise out-of-plane wave vector k_z is unknown because previous ARPES experiments have been carried out with a fixed photon energy [13] that does not allow us to determine k_z. This prohibits comparison to calculations of the band structure in the CDW phase. Quantitative theoretical understanding of the CDW gap is limited because all electronic-structure calculations are done in the normal phase and therefore fail to explain the CDW gap opening observed by ARPES. The reported Raman spectra of VSe_2 are not in good agreement with one another. The Raman spectra of the normal phase consist of an E_g symmetry mode at 143 cm^{-1} and an A_{1g} symmetry mode at 211 cm^{-1} (see Refs. [17,18]). Other works report only the 211 cm^{-1} mode at 300 K and observe the 143 cm^{-1} mode upon cooling to the incommensurate CDW transition [19]. Below $\sim$80 K, the appearance of new Raman peaks at 50, 62, and 174 cm^{-1} was reported [17] but only the peak at 174 cm^{-1} was confirmed in other experiments [19] and attributed to the commensurate CDW transition. The origin of the 174 cm^{-1} peak has not been explained on the basis of the

---

[*] falke@ph2.uni-koeln.de

[†] gianni.profeta@aquila.infn.it

[‡] grueneis@ph2.uni-koeln.de

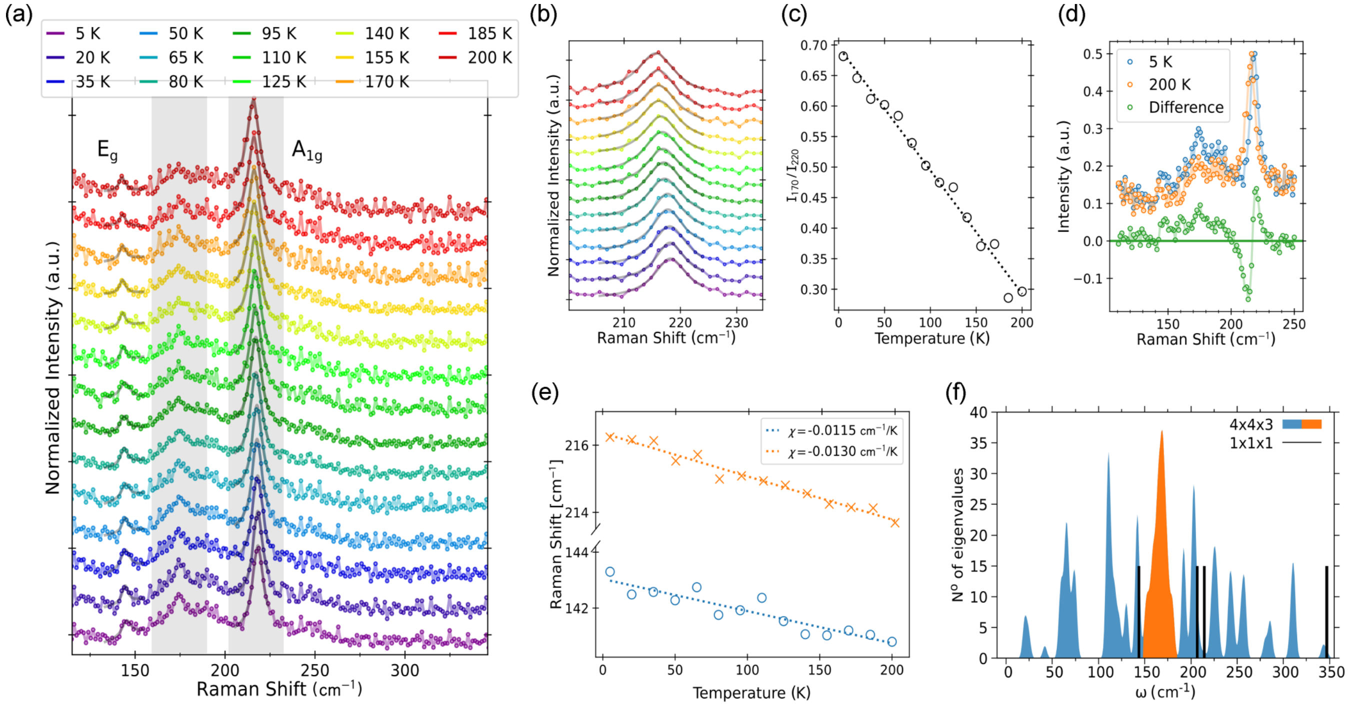

FIG. 1. (a) VSe$_2$ Raman spectra ($\lambda = 633$ nm laser, 0.1 mW, 3600 s integration time per scan) at temperatures between $T = 5 - 200$ K recorded in backscattering geometry at a pressure better than 10^{-5} mbar using a 50x microscope objective. Raman line shapes are fitted by Lorentzians and normalized to the A_{1g} peak. (b) Zoom into the region of the A$_{1g}$ peak showing the experimental spectra and the Lorentzian fits of peak. The Raman scattering geometry was set as follows. The VSe$_2$ layers were in the xy plane and the laser beam was propagating along the z direction. The Raman spectra shown are the sum of $z(xx)z$ and $z(xy)z$ scans (see text). (c) Temperature dependence of the peak positions ω along with a linear fit of frequency versus temperature yielding $\chi = d\omega/dT$. (d) Ratio of integrated Raman intensities from $165 - 185$ cm^{-1} (I_{170}) and $207 - 227$ cm^{-1} (I_{220}), corresponding to grey shaded areas in (a). (e) Raman spectra at 5 K and 200 K with a background subtracted and their difference. (f) Calculated phonon density of states for the normal and CDW phases. The orange area corresponds to the new Raman peak in the range $165 - 185$ cm^{-1}.

phonon dispersion relations. The acoustic phonons of VSe$_2$ have been probed using inelastic X-ray scattering [7] and reveal a phonon softening of the acoustic branch which drives the CDW in agreement with calculations. However, the role of optical phonons in the CDW state, the absence of signatures of EPC in the ARPES spectra, the disagreement in observed CDW gaps, and the poor understanding of the Raman spectra call for a new approach for studying the CDW state. Here, we perform a combined study of the CDW phase of 1T-VSe$_2$ by Raman spectroscopy and ARPES on single crystals of the same batch synthesized via chemical vapor transport using iodine as transport agent [20]. Scanning tunneling microscopy confirms an in-plane 4 × 4 CDW order for our samples [16] and the measured resistance versus temperature has a plateau around 100 K similar to other works [7,19]. We complement our experiments with theoretical studies in the normal and CDW states using density functional theory (DFT). Additionally, we perform tight-binding (TB) calculations to facilitate the assignment of energy bands observed by ARPES to their orbital character and the out-of-plane wave vector.

II. RESULTS

A. Vibrational properties

Raman spectroscopy was performed inside a variable temperature cryostat (Oxford Instruments). It has been noted previously [17] that the weak Raman cross section of VSe$_2$ necessitates long integration times. Temperature-dependent Raman spectra during cooling are shown in Fig. 1(a). The geometry of the Raman experiment was chosen as follows. The layers of VSe$_2$ were in the xy plane, the exciting light had a polarization in the x axis, and we analyzed the scattered light that was polarized in x and in y axis. In the Porto notation, these geometries are $z(xx)z$ and $z(xy)z$ configurations. Here the coordinates in the bracket denote the axes of light polarization and the coordinates outside the brackets denote the axis of the incoming and scattered light.

At all temperatures, we observe three peaks in the energy region between 100 cm^{-1} to 350 cm^{-1}: two peaks at 216.2 cm^{-1} and 143.3 cm^{-1} corresponding to the A_{1g} and E_g symmetry vibrational Raman modes, respectively, and another broad peak that is centered at ~170 cm^{-1}. This is at variance with earlier works reporting that the E_g peak appears below 100 K and the ~170 cm^{-1} peak appears below 40 K [19]. We do not observe peaks at 257 cm^{-1} and 332 cm^{-1} as previously reported [18,19]. There is a very weak intensity feature at 188 cm^{-1} and it could also be related to the CDW phase. However, its intensity is not significantly above noise level and hence it cannot be reliably analyzed. We observe a downshift of the A_{1g} and E_g mode frequencies with increasing temperature. A zoom into the region of the A_{1g} mode is shown in Fig. 1(b) and reveals the temperature-dependent peak shift that is plotted in Fig. 1(c). From a fit of the observed slope of the phonon frequency with temperature and the previously reported temperature dependence of the lattice constants [21], we now experimentally determine the Grüneisen parameters of VSe_2 which have not been reported so far. For the two phonon modes, we have Grüneisen parameter $\gamma_\ell = -V/\omega_\ell \cdot \Delta\omega_\ell/\Delta V$, i.e., $\ell = A_{1g}$ and $\ell = E_g$. In the above definition, ω_ℓ is the phonon frequency and V the volume of the unit cell. We express the relative volume change $\Delta V/V$ in terms of lattice constants a and c and their changes with temperature Δa and Δc as $\Delta V/V = (a^2\Delta c + 2ac\Delta a)/(a^2c)$. We calculate $\Delta V/V$ using $\Delta c/\Delta T = 9 \times 10^{-6}$ ÅK^{-1}, $\Delta a/\Delta T = 18 \times 10^{-6}$ ÅK^{-1}, $a = 3.35$ Å, and $c = 6.10$ Å (at $T = 200$ K) that are obtained from previous x-ray diffraction studies of the lattice expansion [21]. Using our Raman results $\omega_{A_{1g}} = 213.8$ cm^{-1}, $\omega_{E_g} = 140.7$ cm^{-1} (both at $T = 200$ K), $\Delta\omega_{A_{1g}} = -2.5$ cm^{-1}, and $\Delta\omega_{E_g} = -2.3$ cm^{-1} (both for $\Delta T = 195$ K) yields Grüneisen parameters $\gamma_{A_{1g}} = 4.91$ and $\gamma_{E_g} = 6.86$. Upon cooling, the relative intensity of the $\sim$170 cm^{-1} peak increases as can be seen in Fig. 1(a). Figure 1(d) depicts the ratio of the intensities of the peak around 170 cm^{-1} and the A_{1g} peak at $\sim$220 cm^{-1} (I_{170}/I_{220}). The regions used for the integration of Raman intensities are indicated as grey shaded areas in Fig. 1(a). We observe that the I_{170}/I_{220} ratio smoothly increases as temperature is lowered. Figure 1(e) depicts the Raman spectra taken at 5 K and at 200 K and their difference spectrum. The difference spectrum has a peak at $\sim$170 cm^{-1} that is due to the increase in Raman intensity in that energy range upon cooling below the CDW transition temperature. Note that the features at $\sim$220 cm^{-1} in the difference spectrum are due to the temperature induced phonon shift. We performed DFT calculations within the generalized gradient approximation [22] for the exchange-correlation energy and plane-wave expansion with ultrasoft pseudopotentials using QUANTUM ESPRESSO [23]. As cutoff energy, we set 70 (700) Ry for the wave functions (charge density) and performed structural relaxation with a 10 meV/Å threshold. Self-consistent calculations are performed using an unshifted $16 \times 16 \times 10$ electronic mesh and a Marzari-Vanderbilt smearing of 0.01 Ry. Phonon frequencies are calculated by linear response calculation within density-functional perturbation theory [23] on the same electronic mesh and on a $4 \times 4 \times 3$ phonon mesh. DFT yields phonon wave numbers at the zone center of 214.4 cm^{-1} and 143.7 cm^{-1} for the A_{1g} and the E_g modes, respectively. The observed peak at $\sim$170 cm^{-1} has no theory correspondence to a normal phase Γ point phonon. When we compute the phonon density of states at the Γ point in the CDW phase [Fig. 1(f)] we find a peak at $\sim$170 cm^{-1} explaining the Raman observation. Thus, the $\sim$170 cm^{-1} peak is caused by optical phonons with wave vector equal to a quarter of the reciprocal lattice vector which fold back to Γ as a consequence of the 4×4 in-plane superstructure. Let us now compare the experimentally observed Grüneisen parameters with calculations. The experimental values of $\gamma_{A_{1g}} = 4.91$ and $\gamma_{E_g} = 6.86$ agree well to theory yielding $\gamma_{A_{1g}} = 5.24$ and $\gamma_{E_g} = 6.61$. In the calculations of $\gamma_{A_{1g}}$ and γ_{E_g}, the frequency shift induced by the lattice expansion was calculated from the experimental lattice expansion [21] disregarding the Fermi surface change and the CDW transition. This calculation yields frequency shifts of $\Delta\omega_{A_{1g}} = -2.7$ cm^{-1} and $\Delta\omega_{E_g} = -2.26$ cm^{-1} for $\Delta T = 200$ K.

We now discuss the present observation of CDW-related Raman features at temperatures above the critical temperature. Observations of CDW gaps above the critical temperature have been reported previously for VSe_2 and $NbSe_2$. ARPES measurements on VSe_2 by Terashima *et al.* show that the CDW gap has no sharp temperature dependence and that the CDW gap opening persists even above the critical temperature [13]. Similarly, ARPES measurements of the temperature-dependent CDW gap in $NbSe_2$ by Chatterje *et al.* also demonstrate that the CDW gap persists above the critical temperature [24]. Chatterje *et al.* also give an intuitive explanation for their observation. They describe the CDW by a spatially dependent charge density oscillation with a phase. They argue that the phase coherence disappears for temperatures above the critical temperature but the CDW amplitude remains finite. That is, local electronic excitations across the CDW gap can still be observed above the critical temperature but there is no coherent CDW excitation [24]. Our temperature-dependent Raman measurements show a peak whose intensity does not suddenly decrease above the critical temperature but persists above the critical temperature. These measurements are in line with the observations reported by Terashima *et al.* and Chatterje *et al.* and may be explained on the same footing. We point out two more effects that influence the Raman spectra: disorder and two-phonon Raman processes. Disorder generally broadens the CDW transition as a function of temperature. Chatterje *et al.* reported a broadening of the CDW transition as a function of temperature in Mn intercalated $NbSe_2$ from x-ray diffraction measurements [24]. Common defects in VSe_2 such as intercalated V and missing Se atoms may increase the width of the CDW transition. Regarding the phonon origin responsible for the 170 cm^{-1} peak, there might also be a contribution from two-phonon Raman scattering which is distinct from the first-order Raman process described above. It has been shown theoretically by Klein *et al.* that two-phonon Raman scattering is relevant for the Raman spectra of several TMDCs [25]. In the two-phonon Raman process, an electron is photoexcited above E_F and undergoes two subsequent scattering processes with phonons of opposite momenta $\mathbf{q}$ and $-\mathbf{q}$ before recombining with the hole at the wave vector where it was first excited. The corresponding two-phonon Raman peak appears at a frequency which is twice the phonon energy $\hbar\omega(\mathbf{q})$. For the present system, the model by Klein can be tested by substituting the nesting wave vector into the phonon dispersion relations [26]. This yields values of $2\hbar\omega(\mathbf{q}) \sim 110$ cm^{-1}. If we also consider wave vectors with larger magnitude than the nesting vector, the value of $2\hbar\omega(\mathbf{q})$ will increase. Hence the two-phonon Raman scattering involving acoustic phonons may contribute to the broad Raman peak around 170 cm^{-1}.

B. Electron energy band structure

Synchrotron ARPES at variable photon energies is used to determine the inner potential [27] V_0. We obtain $V_0 = 16$ eV and use it to relate photon energy with the out-of-plane wave vector k_z. We perform synchrotron ARPES [28] in the three-dimensional BZ at photon energies between 9 eV and 17 eV in

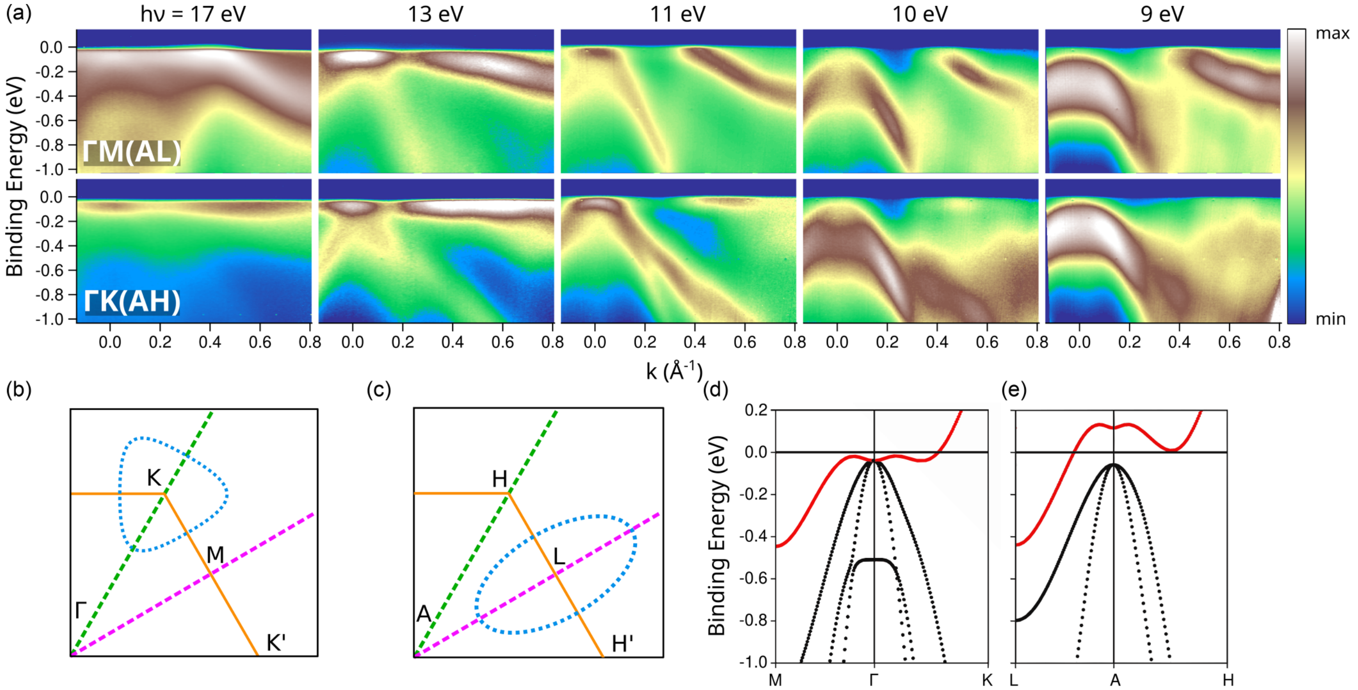

FIG. 2. (a) ARPES ($T = 15$ K) scans along the in-plane high-symmetry directions ΓM (AL) and ΓK (AH) directions shown in the upper and lower panels, respectively, and the ARPES intensity scale. The photon energy $h\nu$ that was used is indicated. For the scan taken at $h\nu = 9$ eV, the out-of-plane wave-vector component at zero in-plane momentum is $k_z = 0.51\,\text{Å}^{-1}$, which corresponds to the A point. The corresponding k_z values for other $h\nu$ are $k_z = 0.48\,\text{Å}^{-1}$ ($h\nu = 10$ eV), $k_z = 0.43\,\text{Å}^{-1}$ ($h\nu = 11$ eV), $k_z = 0.33\,\text{Å}^{-1}$ ($h\nu = 13$ eV), and $k_z = 0.15\,\text{Å}^{-1}$ ($h\nu = 17$ eV). (b) and (c) depict tight-binding calculations of the Fermi surface in the ΓKM and the AHL planes, respectively. The dashed blue areas in (b) and (c) are the hole and electron pockets, respectively. (d) and (e) depict tight-binding calculations of VSe$_2$ (see Ref. [16]) along the $M\Gamma K$ and the LAH directions, respectively, and are useful to identify energy bands in (a). The energy bands with $3d$ and $2p$ character are colored in red and black, respectively.

the two high symmetry in-plane directions $\Gamma(A) - K(H)$ and $\Gamma(A) - M(L)$. The high symmetry points Γ, K, and M have an out-of-plane $k_z = 0$ and A, H, L have $k_z = \pi/c$, where c is the out-of-plane reciprocal lattice vector. The ARPES scans are shown in Fig. 2(a). TB calculations [Figs. 2(b)–2(e)] of the VSe$_2$ band structure are used to assign the observed bands and to confirm the k_z assignment. For the TB calculations, we used a set of parameters that we have previously fit to ARPES data [16]. Guided by the TB calculations, we can identify a rather flat band with $3d$ character close to E_F and three bands with $2p$ character that have a large dispersion and are located close to $\Gamma(A)$. We note that these TB calculations are fit to ARPES experiments [16] and in good qualitative agreement to previous *ab initio* calculations [12]. There is an electron pocket formed by the $3d$ band in the $\Gamma(A) - M(L)$ directions. Its k_z dependence can be probed by varying the photon energy and is understood as follows. In the ΓM direction, the valence band is completely below E_F and hence there is no part of the Fermi surface in this direction. As k_z increases, the valence band moves to higher energies and crosses E_F. In the AL direction, the crossing point of the $3d$ band with E_F is farthest away from the zone center. In the ΓK direction, the $3d$ derived band is flat and as k_z increases, the band moves toward higher energies. In the AHL plane, that band is above E_F. From this three-dimensional band structure analysis follow important constraints for the self-energy analysis that we will perform in a later section. For a self-energy analysis, one desires a sufficiently steep band that is not in proximity to other bands so as to not distort the analysis. We have shown that the $3d$ band in the ΓK and AH directions is flat or above E_F and hence not suitable for a self-energy analysis. That leaves the ΓM and AL directions (and all other k_z values between them). In the ΓM direction, the $3d$ band does not cross E_F but as k_z is increased, the band crosses E_F close to the zone center where other bands are also present. The crossing point of the $3d$ band and E_F is farthest away from the zone center in the AL direction. Therefore, we perform the self-energy analysis in the AHL plane.

C. Charge density wave gap

We performed ARPES in the AHL plane using $h\nu = 67 - 70$ eV [Fig. 3(a)] [29]. The elliptical shapes around the L points are electron pockets of the Fermi surface. High-resolution ARPES scans were performed along lines 1–9 in Fig. 3(a). The corresponding energy distribution curves (EDCs) at points indicated by the orange dots in Fig. 2(a) are shown in Fig. 3(b). There is a suppression in intensity at E_F when moving along the Fermi surface to points further away from the A point. In agreement with an earlier report [14], we associate the ARPES intensity suppression close to E_F with a partial CDW band gap opening. The value of the CDW gap Δ is determined by Lorentzian fits to the EDC curves in an energy range between 60 meV and 5 meV binding energy

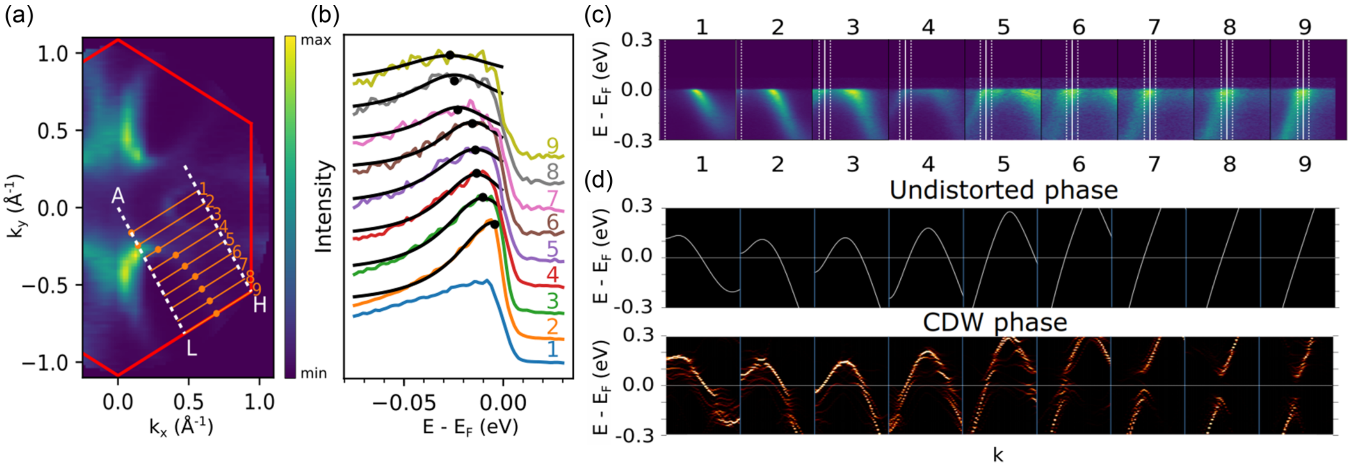

FIG. 3. (a) ARPES equienergy contour map at $E = E_F$ and $T = 8$ K in the AHL plane ($k_z = \pi/c$) for $h\nu = 67$ eV-70 eV and the intensity scale. The parallel lines $1 - 9$ denote the direction of cuts investigated in more detail. (b) Energy distribution curves (EDCs) for lines $1 - 9$ at positions in k space indicated by an orange circle in (a). The black dot above each EDC denotes the maximum ARPES intensity. (c) ARPES cuts along lines 1–9 of (a). The integration range used for the EDCs is indicated. (d) DFT calculations of the band structure along cuts 1–9 for the undistorted (upper panel) and the $4 \times 4 \times 3$ distorted (lower panel) VSe$_2$.

[Fig. 3(b)]. The EDC maxima are shown as black dots in Fig. 3(b). We find the largest Δ for cuts that are close to the L point. For cut 9 in Fig. 3(b), we measure $\Delta = 25 \pm 1$ meV. The value of Δ that we obtain here is smaller than previous ARPES reports that state 80–100 meV [14] and close to the reported 2Δ from STS measurements carried out on the same sample batch [16]. Our ARPES and STS results are reconciled, assuming that the gapped energy region in the conduction band is nearly zero and by the fact that the STS gap is averaged while we here determined the maximum gap. The ARPES intensities along 1–9 are depicted in Fig. 3(c) and show the band that forms the electron pocket around L. The well-defined k_z allows us to perform a detailed comparison to DFT calculations of the spectral function. We perform the calculations in the normal and CDW phases allowing for a one-to-one comparison to the observed CDW gap. The calculations in Fig. 3(d) are for the corresponding cuts shown in Figs. 2(b) and 2(c). The energy range of the gapped region in the DFT calculated spectral function increases for cuts closer to the BZ edge as in the ARPES data. This agreement of theory and experiment highlights that the CDW band gap is a result of zone folding of bands in a 4×4 superstructure, yet the theoretical $\Delta \sim 70$ meV of cut 9 is larger than in the experiment. This may be understood by the small overall energy scale and the fact that our calculation does not include any many-body effects. The CDW gap we present here is solely resulting from zone folding. Nevertheless, our calculations accurately reproduce the experimental trends in Δ as a function of electron wave vector. The zone-folded energy bands hybridize with the original bands resulting in an anticrossing and suppression of the ARPES intensity at E_F [1]. This causes an energy gain of 9.5 meV per formula unit of the normal phase for CDW phase that we calculated in the $4 \times 4 \times 3$ supercell. In VSe$_2$, the zone-folded energy bands have negligible ARPES intensity. This is so because the ARPES intensity of the zone-folded energy bands in ARPES is proportional to the strength of the superperiodic potential which is weak in VSe$_2$.

D. Electron-phonon coupling

We now show the spectral function in the vicinity of the E_F and report a "kink" feature in the AHL plane. We self-consistently analyze the kink, i.e., the noninteracting bare band is chosen such that the real and imaginary parts of the self energy, Re(Σ) and Im(Σ), are Kramers-Kronig related [30,31]. We used data up to 100 meV for the fit and put the constraint that Re(Σ) decreases to zero for energies larger than the phonon energy. The Eliashberg function $\alpha^2F(\omega)$ is obtained via the constraint that the Σ calculated from $\alpha^2F(\omega)$ agrees with the Σ obtained from the self-consistent kink analysis procedure [30,31]. Figure 4(a) depicts the location of points $P1 - P3$ in the AHL plane at which we performed high-resolution ARPES scans that are shown in Fig. 4(b) along with the extracted ARPES maxima and the bare energy band. The kink feature in the maxima of the ARPES data in Fig. 4(b) is best seen for $P2$. Figure 4(c) shows Re(Σ) and Im(Σ), and Fig. 4(d) the fitted $\alpha^2F(\omega)$. For coupling to a single phonon mode, Re(Σ) has a peak at the phonon energy and Im(Σ) has a step at the phonon energy. The present Σ is not composed out of a single phonon mode but is due to a convolution of several phonon modes at different energies, resulting in a broad maximum of Re(Σ) and a smeared out step of Im(Σ). We find that the maximum of Re(Σ) and the step in Im(Σ) are located at 22 meV [Fig. 4(c)]. We will show later that this energy agrees well with optical phonon branches that couple strongly to electrons at E_F. We take into account the broadening induced by coupling to several phonons and modeled the Eliashberg function as the product of a Lorentzian and the phonon frequency ω as $\alpha^2F(\omega) = \omega \cdot \gamma \cdot \alpha^2/[\pi(\omega - \omega_0)^2 + \gamma^2]$. This ensures that $\alpha^2F(\omega) = 0$ for $\omega = 0$ and analytical integrability to obtain the total EPC constant as $\lambda = 2\int \alpha^2F(\omega)/\omega d\omega$ (the integral goes from $\omega = 0$ to ∞). From this analysis, we obtain EPC constants of $\lambda = 0.25$ ($P1$), $\lambda = 0.33$ ($P2$) and $\lambda = 0.34$ ($P3$). These EPC constants are in agreement to point contact spectroscopy which yields an average $\lambda = 0.27$ [32]. The obtained value of λ is less than in related TMDCs that have CDWs, e.g.,

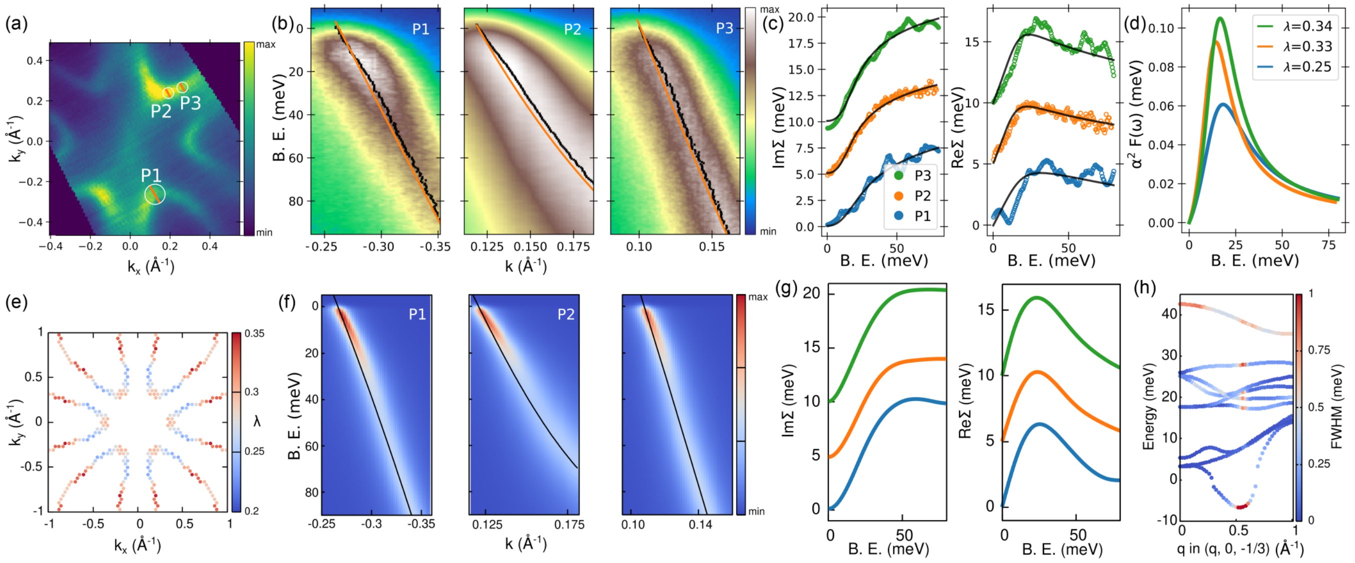

FIG. 4. (a) Fermi surface map in the AHL plane ($h\nu = 37$ eV, $T = 20$ K) showing the location of $P1 - P3$ where electron-phonon coupling (EPC) analysis is performed. (b) ARPES scans along for $P1 - P3$ as a function of binding energy (B.E.). The scan direction is indicated in (a). The black dots indicate the ARPES maxima derived from the momentum dispersion curves and the orange line the bare band. The ARPES intensity scales are shown for (a) and (b). (c) Re(Σ) and Im(Σ) extracted from ARPES ($P1$ and $P3$ data are smoothed and individual scans are upshifted by 5 meV for clarity). The black lines denote Σ calculated from the Eliashberg functions. (d) Eliashberg function $\alpha^2F(\omega)$. The experimentally obtained EPC constants λ for $P1 - P3$ are indicated. (e) Calculated λ along the Fermi surface. (f) Calculated spectral function at $P1 - P3$ and the intensity scale. (g) Theoretical Re(Σ) and Im(Σ). (h) Calculated phonon dispersion relations indicating the full width at half maximum (FWHM) in color. The FWHM is proportional to the inverse phonon lifetime.

for $NbSe_2$ [5] with $\lambda = 0.85$. The relatively small λ in VSe_2 is in line with the absence of superconductivity [8] and the presence of superconductivity in $NbSe_2$ at ambient pressures. We theoretically investigated EPC using the EPW code [33,34] and Wannier interpolation [35] and calculated λ as well as the phonon linewidths. Phonon linewidths are calculated on an interpolated 80 × 80 × 40 electronic mesh. EPC is calculated on a 21 × 21 × 12 phonon mesh. The normal-state Σ is calculated on a 44 × 44 × 24 mesh. Figure 4(e) shows a calculation of λ along the Fermi surface yielding a sizable anisotropy with the largest values of $\lambda = 0.35$ at the most nested wave vectors, in very good agreement with the experiment. Figure 4(f) shows the calculated spectral function along the same path across points $P1 - P3$ as in Fig. 4(b). The solid line denotes the bare band. Figure 4(g) depicts the self-energy extracted from the spectral function at points $P1 - P3$ in excellent agreement with the experimental self-energy, both in terms of the values of Im(Σ) and Re(Σ) and in terms of the location of the peak maximum of Re(Σ) as well as the position of the step in Im(Σ). The phonon dispersion relations in the undistorted phase along q_x, i.e., parallel to AL but shifted to $q_z = \pi/3c$, are plotted in Fig. 4(h). This is the q_z wave-vector plane that drives nesting in the 4 × 4 × 3 CDW phase. The color code of the phonon dispersions indicates the inverse phonon lifetime which is proportional to the contribution to EPC. The negative phonon dispersion branch at $q_x \sim 0.5$ Å^{-1} with a large EPC corresponds to the acoustic phonon that drives the CDW as reported previously [7]. Our calculations additionally reveal optical phonon branches with large EPC at $q_x \sim 0.5$ Å^{-1}. Coupling of electrons close to E_F to these phonon branches explains the kink feature observed in ARPES and the broad Re(Σ) peaked at 22 meV. When these optical branches are zone folded to the center of the BZ in the CDW phase, they can appear in the Raman spectrum provided that they are Raman active. This explains the location of the new Raman peak at 170 cm^{-1} that appears upon cooling, which is at the same energy as the observed kink (1 meV ≈ 8 cm^{-1}).

III. CONCLUSION

In conclusion, our calculations of the electronic structure in the CDW phase reveal gap openings whose wave-vector dependence is in good agreement with ARPES. The CDW phase activates Raman scattering by optical phonons that are Raman forbidden in the normal phase. Electronic coupling to that optical phonon branch is responsible for a kink feature in the spectral function. The EPC pathways that we found are not present in the normal phase and may also play a role for the coexistence of CDW and superconductivity in some TMDCs.

ACKNOWLEDGMENTS

Y.F., N.E., and A.G. acknowledge the ERC Grant No. 648589 SUPER-2D and funding from QM2 as well as CRC1238 (Project No. A1). B.V.S. acknowledges DFG Project No. SE 2575/4-1. We thank Elettra Sincrotrone Trieste for providing access to its synchrotron radiation facilities and the ARPES experiments at the BaDElPh beamline. We acknowledge Diamond Light Source for time on beamline I05 under Proposal No. SI17064. We thank Helmholtz-Zentrum Berlin für Materialien und Energie for the allocation of synchrotron radiation beamtime. EPC measurements were carried out at the 1^2 end-station of UE-112 PGM-2 beamline at the

BESSY II. G.P. acknowledges financial support from the Italian Ministry for Research and Education through PRIN-2017 project Tuning and Understanding Quantum Phases in 2D Materials—Quantum 2D (IT-MIUR Grant No. 2017Z8TS5B). G.M. and G.P. acknowledge support from CINECA Supercomputing Center through the ISCRA project.

---

[1] K. Rossnagel, On the origin of charge-density waves in select layered transition-metal dichalcogenides, J. Phys.: Condens. Matter **23**, 213001 (2011).

[2] D. S. Inosov, V. B. Zabolotnyy, D. V. Evtushinsky, A. A. Kordyuk, B. Büchner, R. Follath, H. Berger, and S. V. Borisenko, Fermi surface nesting in several transition metal dichalcogenides, New J. Phys. **10**, 125027 (2008).

[3] T. E. Kidd, T. Miller, M. Y. Chou, and T.-C. Chiang, Electron-Hole Coupling and the Charge Density Wave Transition in TiSe$_2$, Phys. Rev. Lett. **88**, 226402 (2002).

[4] S. V. Borisenko, A. A. Kordyuk, V. B. Zabolotnyy, D. S. Inosov, D. Evtushinsky, B. Büchner, A. N. Yaresko, A. Varykhalov, R. Follath, W. Eberhardt, L. Patthey, and H. Berger, Two Energy Gaps and Fermi-Surface Arcs" in NbSe$_2$, Phys. Rev. Lett. **102**, 166402 (2009).

[5] T. Valla, A. V. Fedorov, P. D. Johnson, P.-A. Glans, C. McGuinness, K. E. Smith, E. Y. Andrei, and H. Berger, Quasiparticle Spectra, Charge-Density Waves, Superconductivity, and Electron-Phonon Coupling in 2H$-$NbSe$_2$, Phys. Rev. Lett. **92**, 086401 (2004).

[6] M.-A. Méasson, Y. Gallais, M. Cazayous, B. Clair, P. Rodière, L. Cario, and A. Sacuto, Amplitude Higgs mode in the $2H-$NbSe$_2$ superconductor, Phys. Rev. B **89**, 060503(R) (2014).

[7] J. Diego, A. H. Said, S. K. Mahatha, R. Bianco, L. Monacelli, M. Calandra, F. Mauri, K. Rossnagel, I. Errea, and S. Blanco-Canosa, van der Waals driven anharmonic melting of the 3D charge density wave in VSe$_2$, Nat. Commun. **12**, 598 (2021).

[8] S. Sahoo, U. Dutta, L. Harnagea, A. K. Sood, and S. Karmakar, Pressure-induced suppression of charge density wave and emergence of superconductivity in $1T-$VSe$_2$, Phys. Rev. B **101**, 014514 (2020).

[9] K. Tsutsumi, x-ray-diffraction study of the periodic lattice distortion associated with a charge-density wave in $1T$-VSe$_2$, Phys. Rev. B **26**, 5756 (1982).

[10] K. Tsutsumi, T. Sambongi, A. Toriumi, and S. Tanaka, Incommensurate periodic lattice distortion perpendicular to the layer in 1T-VSe$_2$, Physica B+C **105**, 419 (1981).

[11] S. Sugai, Lattice vibrations in the charge-density-wave states of layered transition metal dichalcogenides, Phys. Stat. Sol. B **129**, 13 (1985).

[12] J. Henke, F. Flicker, J. Laverock, and J. van Wezel, Charge order from structured coupling in VSe$_2$, SciPost Phys. **9**, 56 (2020).

[13] K. Terashima, T. Sato, H. Komatsu, T. Takahashi, N. Maeda, and K. Hayashi, Charge-density wave transition of $1T-$VSe$_2$ studied by angle-resolved photoemission spectroscopy, Phys. Rev. B **68**, 155108 (2003).

[14] T. Sato, K. Terashima, S. Souma, H. Matsui, T. Takahashi, H. Yang, S. Wang, H. Ding, N. Maeda, and K. Hayashi, Three-dimensional Fermi-surface nesting in 1T-VSe$_2$ studied by angle-resolved photoemission spectroscopy, J. Phys. Soc. Jpn. **73**, 3331 (2004).

[15] V. N. Strocov, M. Shi, M. Kobayashi, C. Monney, X. Wang, J. Krempasky, T. Schmitt, L. Patthey, H. Berger, and P. Blaha, Three-dimensional electron realm in VSe$_2$ by soft-x-ray photoelectron spectroscopy: Origin of charge-density waves, Phys. Rev. Lett. **109**, 086401 (2012).

[16] W. Jolie, T. Knispel, N. Ehlen, K. Nikonov, C. Busse, A. Grüneis, and T. Michely, Charge density wave phase of VSe$_2$ revisited, Phys. Rev. B **99**, 115417 (2019).

[17] S. Sugai, K. Murase, S. Uchida, and S. Tanaka, Investigation of the charge density waves in IT-VSe$_2$ by Raman scattering, J. Phys. Colloques **42**, C6–740 (1981).

[18] J. E. Smith, J. C. Tsang, and M. W. Shafer, Raman spectra of several layer compounds with charge density waves, Solid State Commun. **19**, 283 (1976).

[19] J. Pandey and A. Soni, Electron-phonon interactions and two-phonon modes associated with charge density wave in single crystalline 1T$-$VSe$_2$, Phys. Rev. Research **2**, 033118 (2020).

[20] K. Nikonov, N. Ehlen, B. Senkovskiy, N. Saigal, A. Fedorov, A. Nefedov, C. Wöll, G. Di Santo, L. Petaccia, and A. Grüneis, Synthesis and spectroscopic characterization of alkali-metal intercalated ZrSe$_2$, Dalton Trans. **47**, 2986 (2018).

[21] G. A. Wiegers, The characterisation of VSe2: A study of the thermal expansion, J. Phys. C **14**, 4225 (1981).

[22] J. P. Perdew, K. Burke, and M. Ernzerhof, Generalized Gradient Approximation Made Simple, Phys. Rev. Lett. **77**, 3865 (1996).

[23] P. Giannozzi, S. Baroni, N. Bonini, M. Calandra, R. Car, C. Cavazzoni, D. Ceresoli, G. L. Chiarotti, M. Cococcioni, I. Dabo, A. Dal Corso, S. de Gironcoli, S. Fabris, G. Fratesi, R. Gebauer, U. Gerstmann, C. Gougoussis, A. Kokalj, M. Lazzeri, L. Martin-Samos, N. Marzari, F. Mauri, R. Mazzarello, S. Paolini, A. Pasquarello, L. Paulatto, C. Sbraccia, S. Scandolo, G. Sclauzero, A. P. Seitsonen, A. Smogunov, P. Umari, and R. M. Wentzcovitch, QUANTUM ESPRESSO: A modular and open-source software project for quantum simulations of materials, J. Phys.: Condens. Matter **21**, 395502 (2009).

[24] U. Chatterjee, J. Zhao, M. Iavarone, R. Di Capua, J. P. Castellan, G. Karapetrov, C. D. Malliakas, M. G. Kanatzidis, H. Claus, J. P. C. Ruff, F. Weber, J. van Wezel, J. C. Campuzano, R. Osborn, M. Randeria, N. Trivedi, M. R. Norman, and S. Rosenkranz, Emergence of coherence in the charge-density wave state of $2H$-NbSe$_2$, Nat. Commun. **6**, 6313 (2015).

[25] M. V. Klein, Theory of two-phonon raman scattering in transition metals and compounds, Phys. Rev. B **24**, 4208 (1981).

[26] J. G. Si, W. J. Lu, H. Y. Wu, H. Y. Lv, X. Liang, Q. J. Li, and Y. P. Sun, Origin of the multiple charge density wave order in $1T-$VSe$_2$, Phys. Rev. B **101**, 235405 (2020).

[27] A. Damascelli, Probing the electronic structure of complex systems by ARPES, Phys. Scr., **T109**, 61 (2004).

[28] L. Petaccia, P. Vilmercati, S. Gorovikov, M. Barnaba, A. Bianco, D. Cocco, C. Masciovecchio, and A. Goldoni, BaD ElPh: A 4m normal-incidence monochromator beamline at Elettra, Nucl. Instrum. Methods Phys. Res. A **606**, 780 (2009).

[29] M. Hoesch, T. K. Kim, P. Dudin, H. Wang, S. Scott, P. Harris, S. Patel, M. Matthews, D. Hawkins, S. G. Alcock, T. Richter, J. J. Mudd, M. Basham, L. Pratt, P. Leicester, E. C. Longhi,

A. Tamai, and F. Baumberger, A facility for the analysis of the electronic structures of solids and their surfaces by synchrotron radiation photoelectron spectroscopy, Rev. Sci. Instrum. **88**, 013106 (2017).

[30] J. Shi, S.-J. Tang, B. Wu, P. T. Sprunger, W. L. Yang, V. Brouet, X. J. Zhou, Z. Hussain, Z.-X. Shen, Z. Zhang, and E. W. Plummer, Direct Extraction of the Eliashberg Function for Electron-Phonon Coupling: A Case Study of Be($10\bar{1}0$), Phys. Rev. Lett. **92**, 186401 (2004).

[31] D. Haberer, L. Petaccia, A. V. Fedorov, C. S. Praveen, S. Fabris, S. Piccinin, O. Vilkov, D. V. Vyalikh, A. Preobrajenski, N. I. Verbitskiy, H. Shiozawa, J. Fink, M. Knupfer, B. Büchner, and A. Grüneis, Anisotropic Eliashberg function and electron-phonon coupling in doped graphene, Phys. Rev. B **88**, 081401(R) (2013).

[32] G. V. Kamarchuk, A. V. Khotkevich, V. M. Bagatsky, V. G. Ivanov, P. Molinié, A. Leblanc, and E. Faulques, Direct determination of Debye temperature and electron-phonon interaction in $1T - \mathrm{VSe}_2$, Phys. Rev. B **63**, 073107 (2001).

[33] F. Giustino, M. L. Cohen, and S. G. Louie, Electron-phonon interaction using Wannier functions, Phys. Rev. B **76**, 165108 (2007).

[34] S. Poncé, E. R. Margine, C. Verdi, and F. Giustino, Epw: Electron-phonon coupling, transport and superconducting properties using maximally localized Wannier functions, Comput. Phys. Commun. **209**, 116 (2016).

[35] A. A. Mostofi, J. R. Yates, G. Pizzi, Y.-S. Lee, I. Souza, D. Vanderbilt, and N. Marzari, An updated version of Wannier90: A tool for obtaining maximally-localised Wannier functions, Comput. Phys. Commun. **185**, 2309 (2014).